This document is downloaded from DR-NTU (https://dr.ntu.edu.sg) Nanyang Technological University, Singapore.

Layer Engineering of 2D Semiconductor Junctions

Li, Bo; Xie, Erqing; He, Yongmin; Sobhani, Ali; Lei, Sidong; Zhang, Zhuhua; Gong, Yongji; Jin, Zehua; Zhou, Wu; Yang, Yingchao; Zhang, Yuan; Wang, Xifan; Yakobson, Boris; Vajtai, Robert; Halas, Naomi J.; Ajayan, Pulickel

2016

He, Y., Sobhani, A., Lei, S., Zhang, Z., Gong, Y., Jin, Z., et al. (2016). Layer Engineering of 2D Semiconductor Junctions. Advanced Materials, 28(25), 5126-5132.

https://hdl.handle.net/10356/83368

https://doi.org/10.1002/adma.201600278

© 2016 WILEY-VCH Verlag GmbH & Co. KGaA, Weinheim. This is the author created version of a work that has been peer reviewed and accepted for publication by Advanced Materials, WILEY-VCH Verlag GmbH & Co. KGaA, Weinheim. It incorporates referee' s comments but changes resulting from the publishing process, such as copyediting, structural formatting, may not be reflected in this document. The published version is available at: [http://dx.doi.org/10.1002/adma.201600278].

Downloaded on 26 Aug 2022 01:39:26 SGT

DOI: 10.1002/((please add manuscript number))

Article type: Communication

Author Manuscript

Title: Layer engineering of 2D semiconductor junctions

Yongmin He, Ali Sobhani , Sidong Lei, Zhuhua Zhang, Yongji Gong, Zehua Jin, Wu Zhou, Yingchao Yang, Yuan Zhang, Xifan Wang, Boris Yakobson, Robert Vajtai, Naomi J. Halas, Bo Li, Erqing Xie*, Pulickel Ajayan**

Y. He, S. Lei, Z. Zhang, Z. Jin, B. Li, Y. Yang, Y. Zhang, X. Wang, B. Yakobson, R. Vajtai, Prof. P. Ajayan

Department of Materials Science and NanoEngineering, Rice University, Houston, Texas, 77005, USA.

E-mail: Bo.Li@rice.edu; ajayan@rice.edu

Y. He, Prof. E. Xie

School of Physical Science and Technology, Lanzhou University, Lanzhou, Gansu, 730000, P. R. China.

E-mail: xieeq@lzu.edu.cn

Z. Zhang

State Key Laboratory of Mechanics and Control of Mechanical Structures, Key Laboratory for Intelligent Nano Materials and Devices of the Ministry of Education, Nanjing University of Aeronautics and Astronautics, Nanjing 210016, China

A. Sobhani, Prof. N. Halas

Department of Electrical and Computer Engineering, Rice University, Houston, Texas, 77005, USA.

Y. Gong

Department of Chemistry, Rice University, Houston, Texas, 77005, USA.

This is the author manuscript accepted for publication and has undergone full peer review but has not been through the copyediting, typesetting, pagination and proofreading process, which may lead to differences between this version and the Version of Record. Please cite this article as doi: 10.1002/adma.201600278.

This article is protected by copyright. All rights reserved.

W. Zhou

Materials Science & Technology Division, Oak Ridge National Lab, Oak Ridge, Tennessee 37831, USA.

Author Manuscript

Keywords: Layer engineering, 2D semiconductor junctions, Multilayer $MoSe_2$, Rectification effects, Photovoltaic effects

Atomically layered 2D materials have attracted significant attention due to their unique thickness-dependent electronic and optical properties.[1-5] Extensive studies have been devoted not only to extending the scientific understanding of atomically layered structures, but also to exploring their applications in electronic devices.[6] These efforts have led to a series of atomically layered electronic and optoelectronic devices,[7-9] including field effect transistors,[10, 11] photovoltaics,[12-16] photo-detectors,[16-19] and nonvolatile memories.[20] Most of these devices are based on junctions, such as p–n junctions[12-15] or Schottky junctions[6].

Here, we introduce a new type of junction specific to 2D layered materials, inspired by their unique, thickness-dependent energy band structure.[21-23] We demonstrate that chemically homogeneous junctions arising from neighboring $MoSe_2$ domains that vary in layer thickness, can also give rise to device behavior. This new type of junction exhibits similar characteristics as p-n junctions, such as rectification and photovoltaics behavior, but without traditional doping strategies[24] or 2D heterojunction fabrication.[12, 15] First-principles calculations show that the layer-dependent band gap

This article is protected by copyright. All rights reserved.

and the Fermi level of few-layered $MoSe_2$ determines the junction behavior. Moreover, our layer-engineered junctions can be fabricated by single step chemical vapor deposition (CVD), in contrast to more complicated processes required for heterogeneous 2D junctions. This principle can be easily extended to other 2D materials, opening up a new pathway for “layer-engineered” device fabrication and design.

In order to obtain 1L-2L (L stands for layer), 2L-3L, and 3L-4L junctions, large-scale $MoSe_2$ layers were grown by CVD under different growth temperatures (More details in Methods Section). As shown in **Figure 1a**, the $MoSe_2$ domains of well-defined numbers of layers can be easily distinguished by their thickness-dependent optical contrast. The domain boundaries in 1-2 layers, 1-3 layers, and 1-4 layers (the second rank in Figure 1a) are uniform and atomically smooth. Note that the CVD method for $MoSe_2$ growth enables a precise control over the number of layers in addition to creating numerous junctions along the edge of the domains on top of the bottom $MoSe_2$ layer. This provides flexibility for the construction of large-scale functional devices and circuits.

We performed atomic force microscopy (AFM) and aberration-corrected scanning transmission electron microscopy (STEM) to investigate the atomic-level nature of the connections between neighboring domains. Figure 1b shows the AFM image of a typical three-layered CVD-grown $MoSe_2$ crystal on a SiO_2/Si substrate. Each domain exhibits excellent uniformity as well as a sharp transition at the edges of the crystal. The height of each domain was measured along the corresponding line scans (Figure S1). A high-resolution AFM scan of the 1L-2L boundary indicates a height difference of approximately 0.7 nm at the junction barrier, confirming a one-layer thickness difference (Figure 1c). In high-angle annular dark field (HAADF) STEM images, the intensity is directly related to the averaged atomic number and the sample thickness. The expected hexagonal structure of single

Author Manuscript

This article is protected by copyright. All rights reserved.

layered $MoSe_2$ (bottom layer) is clearly shown in Figure 1d, where the alternating brighter (Se_2) and darker (Mo) sites are distinguishable in the HAADF images and the intensity profile (red rectangular box) is shown (Figure 1e). The stacking order between layers and the junction region were also characterized by STEM (Figure 1f, Figure S2, Figure S3, and Figure S4). From Figures S2 and S3, it can be seen that our as-grown bilayer and trilayer $MoSe_2$ domains shows 3R stacking. A close inspection of the junction area between neighboring domains reveals an atomically sharp domain boundary (Figure 1 f and Figure S4), where abrupt image contrast variation across the step edges can be clearly observed. The intensity line profile crossing neighboring layers (Figure 1g), shows that the overall roughness of the junction is just less than one unit cell. Our results confirm that CVD growth has produced atomically sharp domain boundaries, a requirement for further investigation on the intrinsic junctions in multilayer $MoSe_2$.

To probe the changes in lattice vibration mode and band structure across $MoSe_2$ domains with different thicknesses, we studied the structures by Raman and PL spectroscopy. **Figure 2a** shows a $MoSe_2$ map for different thicknesses for Raman mapping. The spectra collected from monolayer, bilayer, trilayer, and their respective step edges (marked as points 1 to 5 in Figure 2a), respectively, are shown in Figure 2b. Two main characteristic peaks, at 241 cm^{-1} (A_{1g} mode of $MoSe_2$: out-of-plane vibration) and 286.4 cm^{-1} (E_{2g} mode of $MoSe_2$: in-plane vibration), are observed in all of these samples. Additionally, the A_{1g} mode undergoes a red shift from 242.7 cm^{-1} to 241 cm^{-1}, and its intensity increases by a factor of 2 as the number of layers decreases. The softened A_{1g} mode is a result of a diminishing interplanar restoring force[25]. Also, we observed B^1_{2g} mode of $MoSe_2$ located at 352.6 cm^{-1}, which is absent in monolayer, and then present in bilayer and above. The Raman spectra taken from the step edges (points 2 and 4) indicate that there is no other interlayer-

Author Manuscript

This article is protected by copyright. All rights reserved.

interaction at the step edges, except for the Van der Waals force. Figure 2c shows the A_{1g} peak intensity mapping, further confirming the sharp boundary. All of the characterizations based on STEM, and Raman suggest the presence of a sharp and well-defined intrinsic junction in multilayer $MoSe_2$.

PL spectra acquired from five points from monolayer to trilayer, marked in Figure 2d, are shown in Figure 2e. A strong PL peak at 823 nm is observed in the monolayer domain corresponding to the 1.82 eV transition energy of monolayer $MoSe_2$. The intensity decreases significantly with increasing numbers of layers due to the transition from a direct band gap to an indirect band gap semiconductor. The red shift of the peak position from monolayer to trilayer (from 823.5 nm to 832 nm in wavelength) indicates that the band gap decreases as the number of layers increases, which is consistent with our theoretical calculation (shown later). However, at the step edges, we notice there is no abrupt shifting of peak position while large peak intensities change. To further assess the interfacial effect on the step edges, we acquired a refined PL intensity and spatial mapping (the step length of 200 nm) across these regions. They are marked by the rectangles in Figure 2d. Figures 2f and i show the PL mappings at the 1L-2L and 2L-3L step edge regions, respectively, and demonstrate mismatches between PL intensity mapping and position mapping. The PL peak at ~832 nm, characteristic peak of the monolayer domain, can be observed even in the thicker layer region 0.5~1 µm far from the boundary. We attribute this to a long electron-hole pair diffusion resulting from the concentration gradient between different domains.[26] The electron-hole pair concentration in the monolayer domain is higher than that in the bilayer domain. A similarly extended PL region also exists at the 2L-3L junction.

Author Manuscript

This article is protected by copyright. All rights reserved.

A set of devices was fabricated across 1L-2L, 2L-3L, and 3L-4L domains, respectively, as shown in **Figure 3a** (and Figure S5). In Figure 3b, the junction crossing the 1L-2L domains, in which the monolayer serves as the cathode and the bilayer serves as the anode, exhibits a diode-like rectification behavior. With a forward bias of 10V, 0.1 nA current can pass through the device, whereas a -0.0023 nA current is obtained with a reverse bias of -10 V, the $I_{forward}/I_{reverse}$ ratio of 81 demonstrating a good rectification character. The 2L-3L junction has a similar rectification performance, with the bilayer domain as the cathode and the trilayer domain as the anode. A decreasing trend in rectification behavior from the 1L-2L junction to the 2L-3L junction can be observed; the rectification eventually becomes negligible for the 3L-4L junction (Figure S5).

To elucidate the rectification behavior defined by the number of layers, we performed first-principles electronic structure calculations based on density-functional theory (DFT).[22, 27] Since the rectification behavior is strongest for the 1L-2L junction, we focus first on this case. Figure 3d shows the band structure of a 1L-2L junction. The bands projected to the atoms in the monolayer region form a direct band gap of 1.48 eV and the bands projected to the atoms in the bilayer region form an indirect band gap of 1.18 eV, consistent with the results for the freestanding monolayer and bilayer $MoSe_2$, respectively (Figure S6). Therefore, the local electronic properties in the monolyer and bilayer domains remain essentially unchanged upon junction formation, as proved by our PL measurments. More importantly, the band alignment between the two domains is illustrative of a type II junction with the conduction band minimum (CBM) located on the monolayer and the valance band maximum situated on the bilayer. The band offset in the junction is ~0.4 eV larger than those of previously reported vertical heteorstructures based on 2D metal dichalcogenides[28]. The band offset delivers a built-in electric field pointing from the bilayer to the monolayer, which

Author Manuscript

This article is protected by copyright. All rights reserved.

supports our measurments. Similar behavior also exists for thicker junctions, where the band offset decreases as the number of layers increases. The band offset in the 2L-3L junction is decreased to 0.2 eV, which results in a lower rectification ratio as mentioned above.

It is worth mentioning that we also investigated the metal-semiconductor contact between $MoSe_2$ and Au/Ti electrode. It was found that the Au/Ti electrode tends to form Ohmic contact with thicker $MoSe_2$ domains, for mono-layer part, a weak Schottky contact was observed (Figure 76 a-b). However, the existence of the Schottky junction will not affect the confirmation of the junction between domains with different thicknesses. From the simulation and experiment results, we confirm that the thicker domain serves as anode, and thinner part serves as cathode. Considering the Schottky junction between electrode and $MoSe_2$ (mainly between electrode and monolayer $MoSe_2$), metal electrode should serve as anode and $MoSe_2$ should serve as cathode. In this case the diode formed by thickness dependent domains and the Schottky junction should sit back to back (Figure S7 d). In our experiment, it was confirmed that the rectification behavior from thickness dependent diode dominated. The only issue caused by this Schottky contact is that the photovoltaic effect can be attenuated by it.

We further analyzed this junction by photocurrent and photovoltage response mapping (more details in Methods Section), as shown in **Figure 4 a-d**. As we can see from Figure 4a and b, the photovoltaic effect is mainly located along the step edge between monolayer and bilayer domains, and there is no photovoltage response near the metal electrodes. This result indicates that the thickness-dependent built-in electric field in our device is derived from the step edge between the different thickness domains, rather than the Schottky junction between metal electrode and $MoSe_2$, if one is present. Also, it is the direct experimental evidence that there exist intrinsic “layer

Author Manuscript

This article is protected by copyright. All rights reserved.

engineering" semiconductor junctions in multilayer $MoSe_2$. As shown in the photocurrent mappings (Figure 4c,d), under forward bias voltage, only the monolayer has a photoresponse, whereas only the bilayer has a photoresponse under reverse bias voltage. This phenomenon can be explained by the band structure alignment across the intrinsic junction under different bias voltages (Figure 4e,f). With a forward bias voltage, a higher potential barrier forms in the valence band edge due to the disparity between the band levels at the junction. Therefore, any holes generated in the bilayer could not pass through it, resulting in no photoresponse in this region, as shown in Figure 4f. Under reverse bias voltage, the band offsets increase (Figure 4e) and facilitate the separation of photogenerated carriers (electron and hole) in both monolayer and bilayer drifting due to their corresponding electrodes (positive and negative). Hence both monolayer and bilayer should deliver a photoresponse, although this is not the case in our experimental observation.

To clarify this issue, we detected the photoresponse of an individual single layer and a bilayer near the junction as well as far from the junction (Figure S8). The results raised two questions. First, why did the monolayer with a direct bandgap deliver a weak photoresponse as well as the bilayer (indirect bandgap) far from junction? We attribute this to the high absorption coefficient in the bilayer leading to a large quantum yield, similar to MoS_2.[29] Second, why did the bilayer near the junction deliver a much stronger photoresponse than that of the bilayer far from the junction? It appears possible that the bilayer near the junction, namely near the region of built-in electrical field, has much more photo-generated carrier (electron-hole pair) separated efficiently, compared to the region far from the junction. Therefore, we suggest that under reverse bias voltage (Figure 4c), the larger quantum yield of the bilayer effectively contributes to a much larger photocurrent than that of the monolayer.

Author Manuscript

This article is protected by copyright. All rights reserved.

Besides rectification behavior, we observed an open circuit voltage (OCV) of 148 mV from the 1L-2L junction (**Figure 5a**), which is comparable to other 2D photovoltaic devices[12-15, 30]. Meanwhile, the 2L-3L junction delivers an OCV of 46 mV, and a much smaller open circuit voltage for the 3L-4L junction. This trend is similar to that in the rectification behaviors of these junctions, and can be explained by our theoretical analysis that as the number of layers increase, the band offset decreases. Note that we also measured the photovoltaic response along the 1L-2L and 2L-3L junctions, and no apparent photovoltaic response was observed (Figure S9). Our results show that photovoltaic effects only occur across the neighboring layer junction but not along the junction. Note that the photo-thermoelectric effect also leads to an open circuit voltage for TMDCs materials[31], thus we also evaluated the photo-thermal voltage based on 1L-2L junction in multilayer $MoSe_2$ (Supporting Information). At room temperature and zero gate voltage, this value is smaller than 10 mV. If we compare this photo-thermal voltage value to the measured open-circuit voltage of 148 mV, it is clear that the photo-thermal contribution is very much smaller compared to the photovoltaic effect.

Figure 5b shows the I-V characteristic and the output power of a 1L-2L junction. As the output current increases, the voltage drops due to the inner impedance of the device, and the short circuit current is 76.6 pA. The output power (green curve) reaches a maximum power of 3.15 pW at a voltage of 85 mV with a current of 37 pA, corresponding to a fill factor of 0.28. An integrated four-unit solar cell array was created by patterning 1L-2L junctions in series, as shown in Figure 5c. A superposition of OCV can be observed as the number of cells increases (Figure 5d). This result indicates that the thickness-dependent junction network can possess a high open circuit voltage, by increasing the number of in-series devices.

Author Manuscript

This article is protected by copyright. All rights reserved.

In summary, we fabricated 2D junctions based on atomically layered $MoSe_2$ with varying numbers of layers. The type of junction in $MoSe_2$ can be engineered by utilizing different numbers of layers, which is only possible in super thin layered 2D materials, due to the layer-dependent band structure of these materials. More importantly, many junctions can be easily produced via layer-controllable large-scale CVD growth. This allows a unique approach for creating semiconductor junctions and devices, in contrast to current methods of constructing p-n or Schottky junctions based on 2D materials that require deliberate alignment, stacking or doping. Our results could pave a new pathway for the design of new types of device architectures based on chemically homogenous semiconductor junctions.

Author Manuscript

This article is protected by copyright. All rights reserved.

Experimental Section

Synthesis of multilayer $MoSe_2$

Molybdenum trioxide (MoO_3) (99%, Sigma Aldrich) powder and selenium (Se) (99.5%, Sigma Aldrich) powder were employed as the precursor and a clean SiO_2 (275 nm)/Si wafer was used as the growth substrate. The growths for different layer numbers use the same amount of chemicals i.e. 20 mg MoO_3 and 150 mg Se. A mixture of argon and hydrogen (15% hydrogen) (Ar, ultra high purity, 99.999%. H_2, ultra high purity, 99.999%) served as carrier gas, in which the small fraction of H_2 would facilitate $MoSe_2$ nucleation and growth by promoting Se to reduce MoO_3. The growth temperature was kept at 750-900°C, and at the same time Se powder was loaded upstream at approximately 200°C. The flow rate is 50 SCCM for all growth and the reaction chamber is at atmospheric pressure. The ramping time from room temperature to growth temperature is 15 min and the growth time (selenization time) is 20 min. The thickness of the $MoSe_2$ sample can be controlled by the growth temperature. In order to realize the multilayer nucleation of $MoSe_2$, higher temperatures are necessary. For CVD growth of multilayer $MoSe_2$, high temperature can introduce a thermodynamic process comparing to a kinetic process at low temperature,[32] which is a general case for temperature selective growth in chemistry.[33] At high temperature, upper triangles usually grow from the same nucleation site at the center of the bottom triangle for multilayer $MoSe_2$. In our experiment, growth at 750°C would yield $MoSe_2$ dominated by monolayer, while 825°C and 900°C can result in bilayer and 3-4 layers samples, respectively.

Characterization of Multilayer $MoSe_2$ Structure

Author Manuscript

This article is protected by copyright. All rights reserved.

The microstructures and morphologies based on multilayer $MoSe_2$ were characterized by optical microscope, AFM (Agilent PicoScan 5500 and Veeco Digital Instrument Nanoscope IIIA), STEM (a Nion UltraSTEM-100, at an accelerating voltage of 60 kV), and Raman and PL spectroscopies (Renishaw inVia). The AFM measurements were performed using Bruker 8 AFM microscope system under ScanAsyst mode, and both Raman and PL spectroscopies were tested by a 514.5 nm laser (with spot size about 1μm in diameter) under room temperature.

Electrical and Photoelectric Measurements of the Semiconductor Junctions in Multilayer $MoSe_2$

The rectification, photoconductivity and photovoltaics studies were performed using a home-built probe-station under 2×10^{-5} torr. All of the devices based on junctions between neighboring $MoSe_2$ layers were fabricated using electron-beam lithography followed by electron-beam deposition of metal contact electrodes (5/50 nm). The devices were powered with a Keithley 2634B dual-channel source meter unit connected to the probe station with a triaxial cable for low-noise measurement. A 543 nm He-Ne laser with an intensity 100±2 mW/cm^2 was utilized as excitation source for photoconductivity and photovoltaic studies.

For the photocurrent and photovoltage mappings, each device was illuminated by a focused monochromic laser which was generated from a supercontinuum fiber laser (Fianium) followed by an acousto-optical tunable filter (Crystal Tech.) for wavelength selection. The monochromic laser was chopped for modulation and a lock-in amplifier (Signal Recovery, 7280DSP) locked to the chopping frequency was applied for the measurement. Note that, during the photovoltage mapping the measurement, the lock-in amplifier inset a very large input resistance (giga ohms) in the circuit, so that no significant current was passing the device, so the signal would not be changed by the

Author Manuscript

This article is protected by copyright. All rights reserved.

other components of the device. Thus, we employed this method to in situ measure the photoelectric response precisely. For the resolution of the mapping, the spot size (waist of the Gaussian beam) of the focused laser was measured to ~ 1μm in diameter. By carefully moving the laser beam in space (in order to keep the laser power consistent for all pixels), the actual resolution of the measurements is about 1 μm. But, since the focused laser beam has a Gaussian profile and it has a higher intensity at the center of the laser dot, the maps actually still give an understanding for step sizes lower than 1 μm.

Theory Calculation of the Junction

First-principles calculations were performed with the Vienna Ab-initio Simulation Package (VASP)[34, 35], using the projector-augmented wave method for the core region and DFT based on local density approximation with a plane-wave kinetic energy cutoff of 350 eV. A vacuum layer of 20 Å isolates neighboring periodic images. The 1L-2L junction is simulated by placing an armchair $MoSe_2$ nanoribbon (the width is half of the supercell dimension) on a monolayer MoS_2, and the 2L-3L junction is simulated by placing a narrower armchair $MoSe_2$ nanoribbon on the 1L-2L system. We calculated the bands projected to the monolayer, bilayer, and trilayer domains to examine their electronic properties. All atomic positions are relaxed using conjugate-gradient techniques until the force on each atom is less than 0.01 eV/Å. The band offset over the junctions is obtained by fitting the curve of the band edge versus width of the ribbons (the ratio of ribbon width and the supercell dimension is kept 1:2, see details in Figure S6).

Author Manuscript

This article is protected by copyright. All rights reserved.

Author Manuscript

Supporting Information

AFM characterization of a typical $MoSe_2$ trilayer, Z-contrast images of 1L-2L and 2L-3L junctions region; I-V curves of the device based 3L-4L junction, and individual monolayer, bilayers, and trilayer; Photo-response based on individual monolayer, bilayer near the junction and far from the junction, the 1L-2L and 2L-3L junction with a parallel direction along junction; Supporting Information is available from the Wiley Online Library or from the author.

Acknowledgements

This work is supported by FAME, one of six centers of STARnet, a Semiconductor Research Corporation program sponsored by MARCO and DARPA. Y.H. acknowledges the financial support from China Scholarship Council. This work is also supported by the Fundamental Research Funds for the Central Universities in China (lzujbky-2015-303).

Electron microscopy study was supported by the U.S. Department of Energy, Office of Science, Basic Energy Science, Materials Sciences and Engineering Division (WZ), and through a user project at ORNL's Center for Nanophase Materials Sciences (CNMS), which is a DOE Office of Science User Facility.

Received: ((will be filled in by the editorial staff))
Revised: ((will be filled in by the editorial staff))
Published online: ((will be filled in by the editorial staff))

This article is protected by copyright. All rights reserved.

[1] Q. H. Wang, K. Kalantar-Zadeh, A. Kis, J. N. Coleman, M. S. Strano, *Nat. Nanotechnol.*, **2012**, *7*, 699.

[2] V. Nicolosi, M. Chhowalla, M. G. Kanatzidis, M. S. Strano, J. N. Coleman, *Science*, **2013**, *340*.

[3] A. K. Geim, I. V. Grigorieva, *Nature*, **2013**, *499*, 419.

[4] M. Xu, T. Liang, M. Shi, H. Chen, *Chemical Reviews*, **2013**, *113*, 3766.

[5] M. Chhowalla, H. S. Shin, G. Eda, L.-J. Li, K. P. Loh, H. Zhang, *Nat. Chem.*, **2013**, *5*, 263.

[6] S. Z. Butler, S. M. Hollen, L. Cao, Y. Cui, J. A. Gupta, H. R. Gutiérrez, T. F. Heinz, S. S. Hong, J. Huang, A. F. Ismach, E. Johnston-Halperin, M. Kuno, V. V. Plashnitsa, R. D. Robinson, R. S. Ruoff, S. Salahuddin, J. Shan, L. Shi, M. G. Spencer, M. Terrones, W. Windl, J. E. Goldberger, *ACS Nano*, **2013**, *7*, 2898.

[7] D. Jariwala, V. K. Sangwan, L. J. Lauhon, T. J. Marks, M. C. Hersam, *ACS Nano*, **2014**, *8*, 1102.

[8] D. Lembke, S. Bertolazzi, A. Kis, *Acc. Chem. Res.*, **2015**, *48*, 100.

[9] R. Ganatra, Q. Zhang, *ACS Nano*, **2014**, *8*, 4074.

[10] RadisavljevicB, RadenovicA, BrivioJ, GiacomettiV, KisA, *Nat. Nanotechnol.*, **2011**, *6*, 147.

[11] S. Das, H.-Y. Chen, A. V. Penumatcha, J. Appenzeller, *Nano Lett.*, **2013**, *13*, 100.

[12] C.-H. Lee, G.-H. Lee, A. M. van der Zande, W. Chen, Y. Li, M. Han, X. Cui, G. Arefe, C. Nuckolls, T. F. Heinz, J. Guo, J. Hone, P. Kim, *Nat. Nanotechnol.*, **2014**, *9*, 676.

[13] A. Pospischil, M. M. Furchi, T. Mueller, *Nat. Nanotechnol.*, **2014**, *9*, 257.

[14] J. S. Ross, P. Klement, A. M. Jones, N. J. Ghimire, J. Yan, D. G. Mandrus, T. Taniguchi, K. Watanabe, K. Kitamura, W. Yao, D. H. Cobden, X. Xu, *Nat. Nanotechnol.*, **2014**, *9*, 268.

[15] M. M. Furchi, A. Pospischil, F. Libisch, J. Burgdörfer, T. Mueller, *Nano Lett.*, **2014**, *14*, 4785.

[16] B. W. H. Baugher, H. O. H. Churchill, Y. Yang, P. Jarillo-Herrero, *Nat. Nanotechnol.*, **2014**, *9*, 262.

[17] F. H. L. Koppens, T. Mueller, P. Avouris, A. C. Ferrari, M. S. Vitiello, M. Polini, *Nat. Nanotechnol.*, **2014**, *9*, 780.

[18] K. Roy, M. Padmanabhan, S. Goswami, T. P. Sai, G. Ramalingam, S. Raghavan, A. Ghosh, *Nat. Nanotechnol.*, **2013**, *8*, 826.

Author Manuscript

This article is protected by copyright. All rights reserved.

[19] O. Lopez-Sanchez, D. Lembke, M. Kayci, A. Radenovic, A. Kis, *Nat. Nanotechnol.*, **2013**, *8*, 497.

[20] S. Bertolazzi, D. Krasnozhon, A. Kis, *ACS Nano*, **2013**, *7*, 3246.

[21] K. F. Mak, C. Lee, J. Hone, J. Shan, T. F. Heinz, *Phys. Rev. Lett.*, **2010**, *105*, 136805.

[22] J. Kang, S. Tongay, J. Zhou, J. Li, J. Wu, *Appl. Phys. Lett.*, **2013**, *102*, 012111.

[23] G. Eda, H. Yamaguchi, D. Voiry, T. Fujita, M. Chen, M. Chhowalla, *Nano Lett.*, **2011**, *11*, 5111.

[24] S. Wi, H. Kim, M. Chen, H. Nam, L. J. Guo, E. Meyhofer, X. Liang, *ACS Nano*, **2014**, *8*, 5270.

[25] S. Horzum, H. Sahin, S. Cahangirov, P. Cudazzo, A. Rubio, T. Serin, F. M. Peeters, *Phys. Rev. B*, **2013**, *87*, 125415.

[26] N. Kumar, Q. Cui, F. Ceballos, D. He, Y. Wang, H. Zhao, *Nanoscale*, **2014**, *6*, 4915.

[27] J. He, K. Hummer, C. Franchini, *Phys. Rev. B*, **2014**, *89*, 075409.

[28] J. Yuan, S. Najmaei, Z. Zhang, J. Zhang, S. Lei, P. M. Ajayan, B. I. Yakobson, J. Lou, *ACS Nano*, **2015**, *9*, 555.

[29] K. F. Mak, C. Lee, J. Hone, J. Shan, T. F. Heinz, *Phys. Rev. Lett.*, **2010**, *105*, 136805.

[30] M. Fontana, T. Deppe, A. K. Boyd, M. Rinzan, A. Y. Liu, M. Paranjape, P. Barbara, *Sci. Rep.*, **2013**, *3*.

[31] M. Buscema, J. O. Island, D. J. Groenendijk, S. I. Blanter, G. A. Steele, H. S. J. van der Zant, A. Castellanos-Gomez, *Chem. Soc. Rev.*, **2015**, *44*, 3691.

[32] Y. Gong, J. Lin, X. Wang, G. Shi, S. Lei, Z. Lin, X. Zou, G. Ye, R. Vajtai, B. I. Yakobson, H. Terrones, M. Terrones, Beng K. Tay, J. Lou, S. T. Pantelides, Z. Liu, W. Zhou, P. M. Ajayan, *Nat. Mater.*, **2014**, *13*, 1135.

[33] A. L. Sargent, M. B. Hall, M. F. Guest, *J. Am. Chem. Soc.*, **1992**, *114*, 517.

[34] G. Kresse, J. Hafner, *Phys. Rev. B*, **1994**, *49*, 14251.

[35] G. Kresse, J. Furthmüller, *Phys. Rev. B*, **1996**, *54*, 11169.

Author Manuscript

This article is protected by copyright. All rights reserved.

Author Manuscript

This article is protected by copyright. All rights reserved.

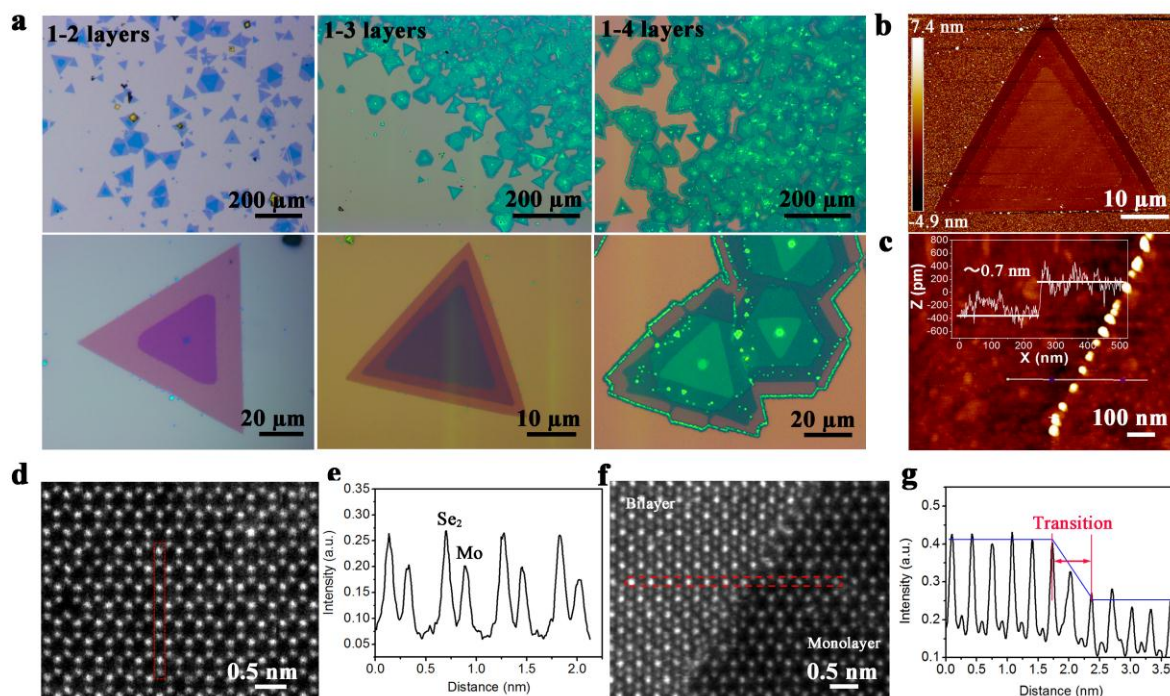

Figure 1 The morphologies of large-scale and layer-controllable CVD growth of $MoSe_2$. (a) Optical images of the CVD growth of 1-2, 1-3, and 1-4 multilayer $MoSe_2$, showing the high yield of $MoSe_2$ multilayers. (b) AFM characterization of a typical $MoSe_2$ trilayer. (c) High-resolution AFM image of the 1L-2L step edge. The inset displays the corresponding line scans. (d) and (e) the STEM-HAADF image (d) of monolayer $MoSe_2$ shows its perfect hexagonal lattice and the intensity profile (e) marked in the red box in d. (f) STEM-HAADF images of the 1L-2L step edge, showing an atomically sharp step. (g) Intensity profile crossing the 1L-2L junction acquired in the red rectangle box in (f).

Author Manuscript

This article is protected by copyright. All rights reserved.

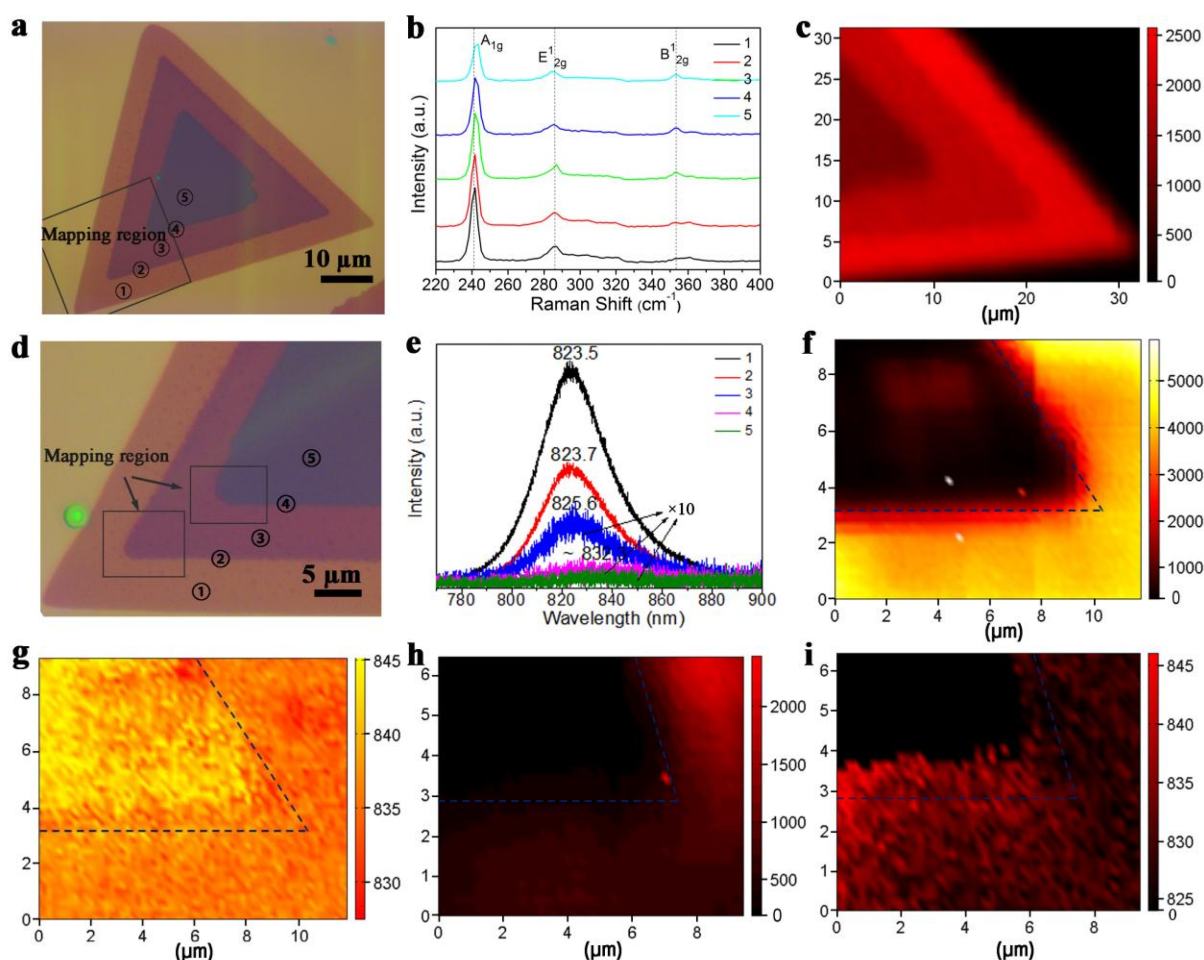

Figure 2. Raman and Photoluminescence characterization of a typical 1-2-3 multilayer $MoSe_2$. (a) Optical image of a 1-2-3 multilayer $MoSe_2$ used for Raman characterization. (b) Raman spectra taken from the five points marked in (a), showing a thickness-dependent A1g mode shift. (c) Raman map of the intensity of the A1g mode collected from the rectangle region in (a). (d) Optical image of a 1-2-3 multilayer $MoSe_2$ used for PL characterization. (e) PL Spectra taken from the five points marked in (d), which shows how the characteristic $MoSe_2$ PL peak intensity greatly decreases and its position undergoes red shift as the number of layer increases. (f) and (g) PL intensity (f) and position (g) maps collected from 1L-2L junction region marked by black rectangle in Figure d. (h) and (i) PL intensity (h) and position (i) maps collected from 2L-3L junction region marked by black rectangle in Figure d. Each step edge in the PL intensity and position maps was marked by a blue dotted line. The blue line demonstrates the mismatch in step edge regions. All scanning micro-photoluminescence and micro-Raman mappings were performed with 514 nm laser excitation at room temperature.

Author

This article is protected by copyright. All rights reserved.

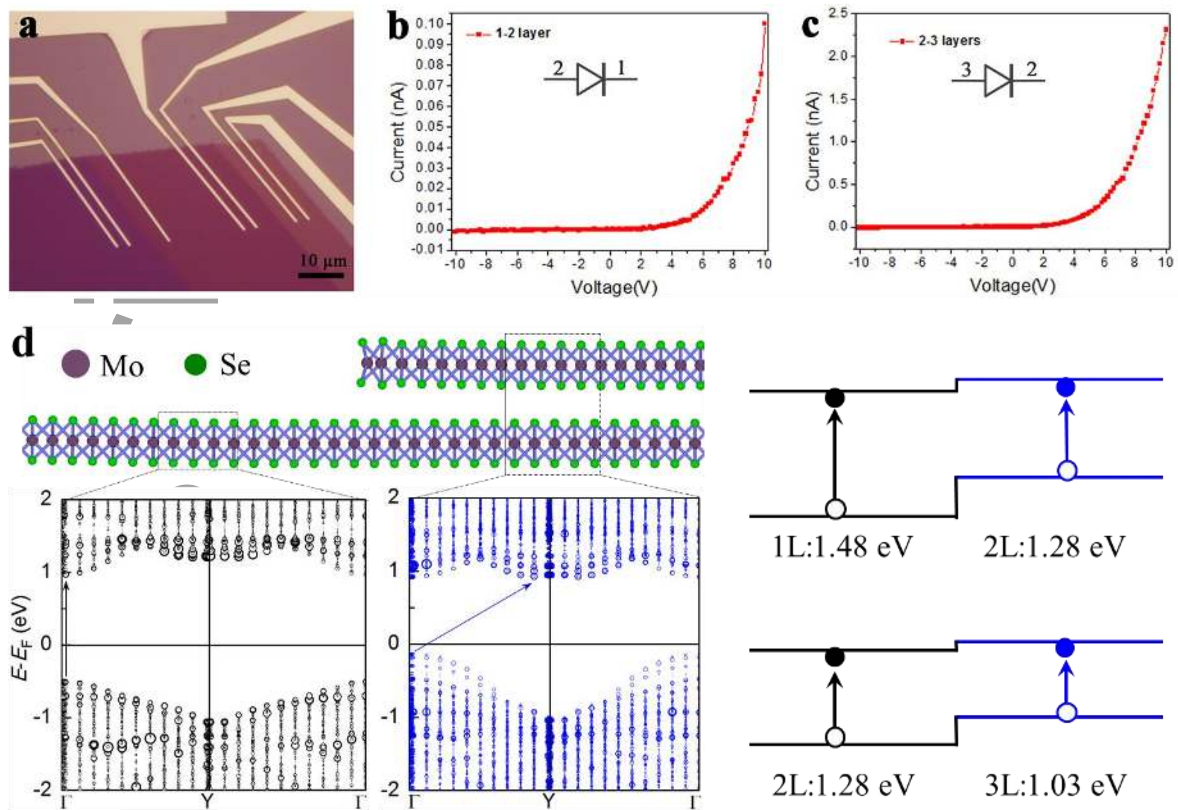

Figure 3 Electrical characterization and theoretical calculations of an intrinsic junction in multilayer $MoSe_2$. (a) Optical image of the devices based on intrinsic junctions in $MoSe_2$ from 1L-2L and 2L-3L domains. (b) and (c): I-V curves of devices based on 1L-2L and 2L-3L junctions. They illustrate the typical diode behaviors. (d) Electronic band structures of 1L-2L and 2L-3L junctions, respectively.

Author Manuscript

This article is protected by copyright. All rights reserved.

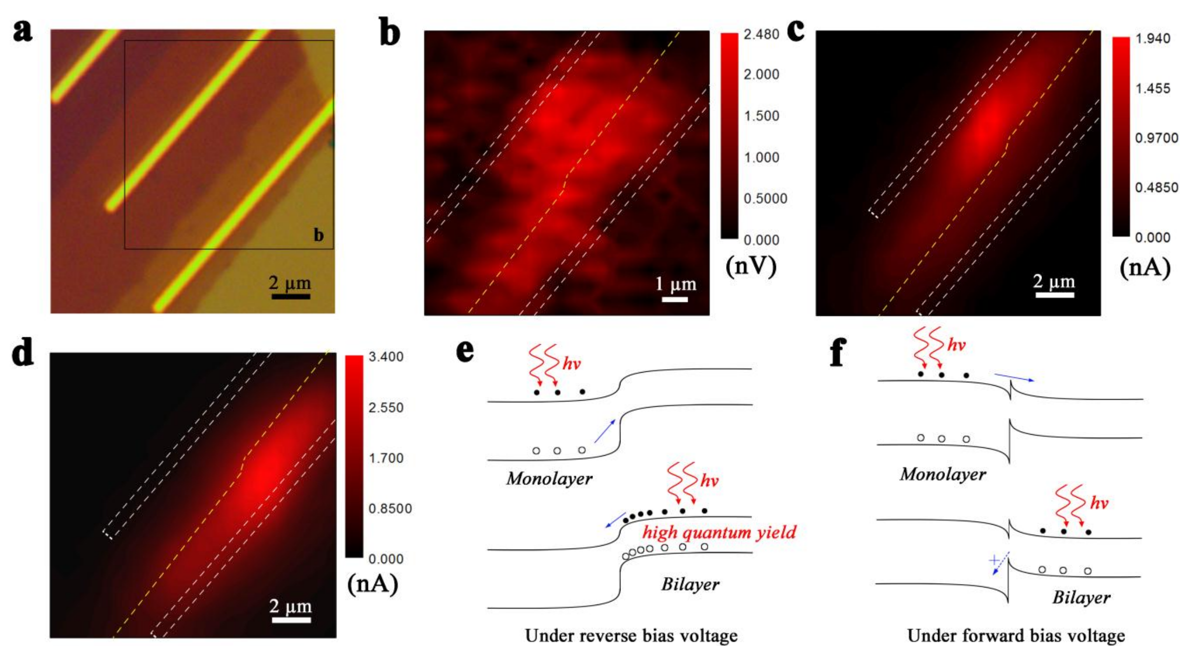

Figure 4 Photoelectronic characterization of the thickness-dependent intrinsic junction in multilayer $MoSe_2$. (a) Optical image of a typical 1L-2L junction device. (b) Scanning photovoltage (open circuit voltage) mapping collected from the rectangle region in (a). (c) and (d) Scanning photocurrent intensity mappings based on (a), under -5V (c) and 5V (d) bias voltages. In all of the mapping images, the white dashed line delineates the metal electrodes, and the yellow dashed line outlines the boundary between the monolayer and bilayer. The color intensity in the mapping images was normalized as intensity. (e) and (f) Band profiles of 1L-2L intrinsic junction under reverse bias voltage (e)and under forward bias voltage (f), respectively.

Author Manuscript

This article is protected by copyright. All rights reserved.

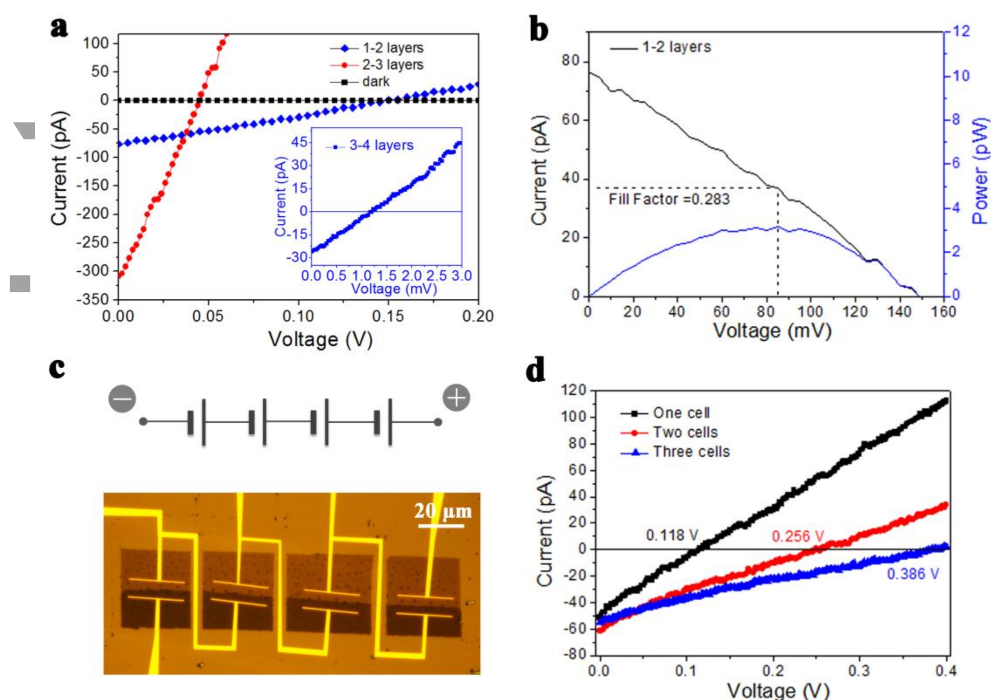

Figure 5 (a) Output characteristics in the configuration based on thickness-dependent intrinsic junctions (1L-2L and 2L-3L junctions) in multilayer $MoSe_2$. The inset shows a weaker output characteristic for the 3L-4L junction. (b) I-V curve of the PV device working as a solar cell based on a 1L-2L junction. (c) Optical image of 4 cells fabricated in series (bottom), and the corresponding circuit diagram (top). (d) Output characteristics of the 4 cells in series based on the 1L-2L junction.

Author Manuscript

This article is protected by copyright. All rights reserved.

The table of contents entry:

Based on this thickness dependence, a new concept for junction fabrication by connecting multiple regions with varying layer thicknesses is demonstrated. This type of junction is only possible in super thin layered 2D materials, and exhibits similar characteristics as p-n junctions. Rectification and photovoltaic effects are observed in chemically homogeneous $MoSe_2$ junctions between domains of different thicknesses.

Keyword: Layer engineering, 2D semiconductor junctions, Multilayer $MoSe_2$, Rectification effects, Photovoltaic effects

Yongmin He, Ali Sobhani , Sidong Lei, Zhuhua Zhang, Yongji Gong, Zehua Jin, Wu Zhou, Bo Li*, Yingchao Yang, Yuan Zhang, Xifan Wang, Boris Yakobson, Robert Vajtai, Naomi J. Halas, Erqing Xie*, Pulickel Ajayan*

Title: Layer engineering of 2D semiconductor junctions

ToC figure

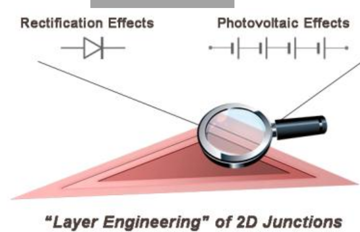

Author Manuscript

This article is protected by copyright. All rights reserved.

Copyright WILEY-VCH Verlag GmbH & Co. KGaA, 69469 Weinheim, Germany, 2013.

Supporting Information

Title: Layer engineering of 2D semiconductor junctions

Yongmin He, Ali Sobhani , Sidong Lei, Zhuhua Zhang, Yongji Gong, Zehua Jin, Wu Zhou, Bo Li, Yingchao Yang, Yuan Zhang, Xifan Wang, Boris Yakobson, Robert Vajtai, Naomi J. Halas, Erqing Xie*, Pulickel Ajayan**

Author Manuscript

This article is protected by copyright. All rights reserved.

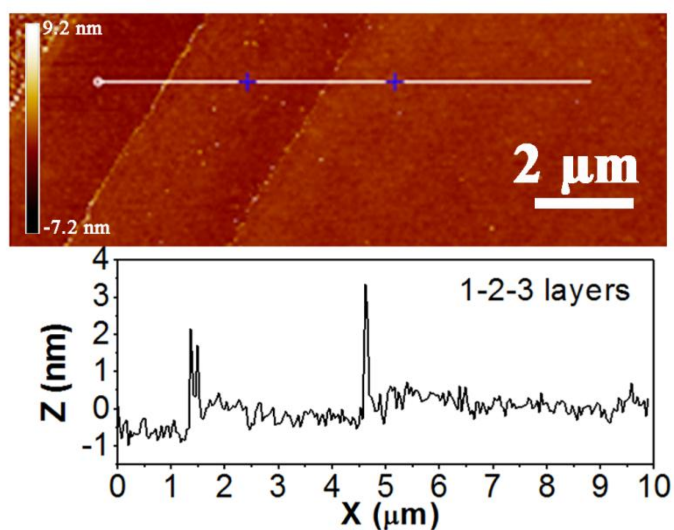

Figure S1. AFM characterization of a typical $MoSe_2$ trilayer and a representative line profile, showing a well-defined single trilayer domain.

Author Manuscript

This article is protected by copyright. All rights reserved.

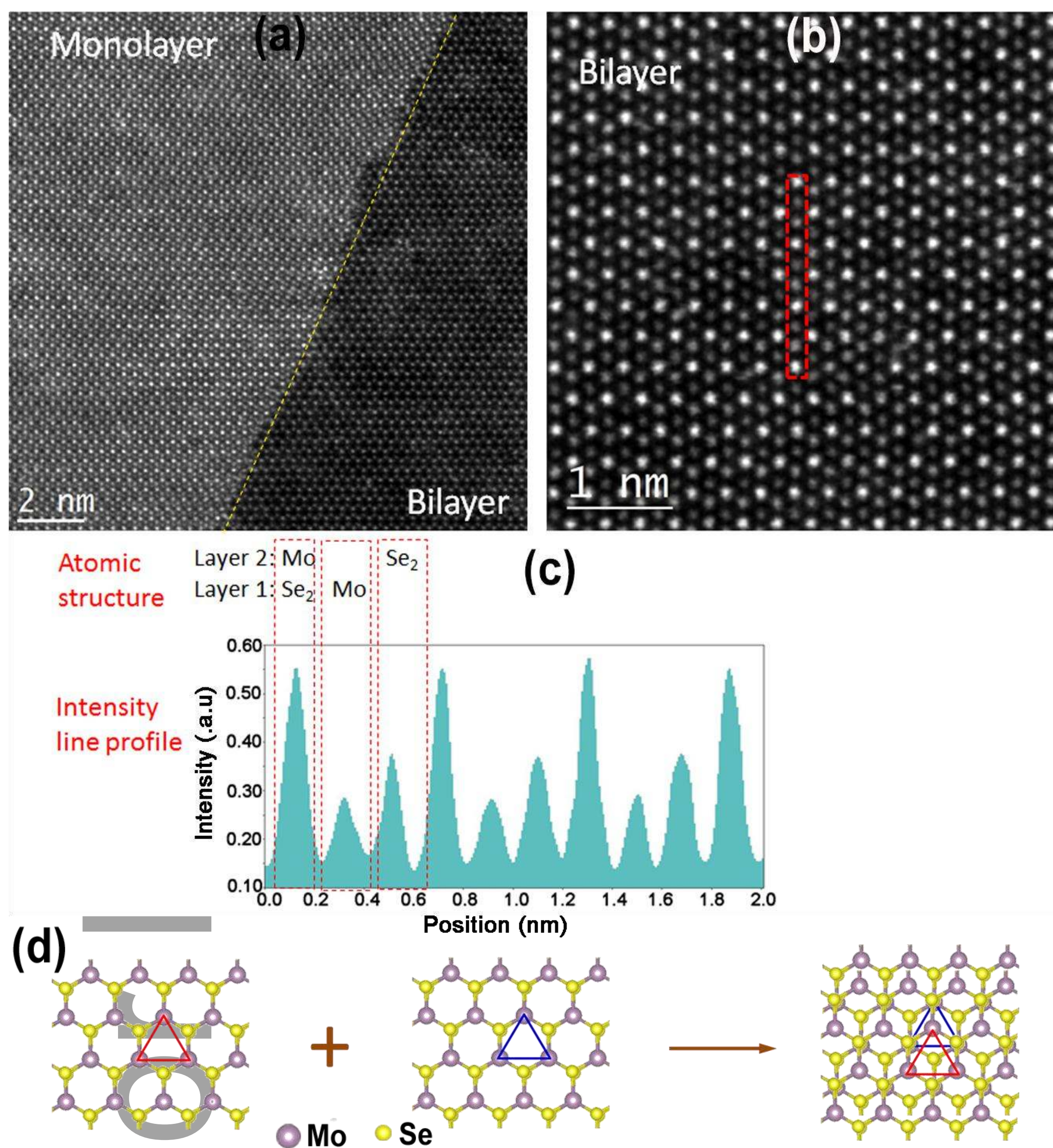

Figure S2. Z-contrast image of the 1-2 layer junction region (a) and bilayers (b) collected from 1-2 layer junction region. (c) Image intensity profile acquired along the red rectangle in the Z-contrast image above, and its corresponding stack schematic (d), indicating a 3R stacking in bilayer domain.

Author

This article is protected by copyright. All rights reserved.

Author Manuscript

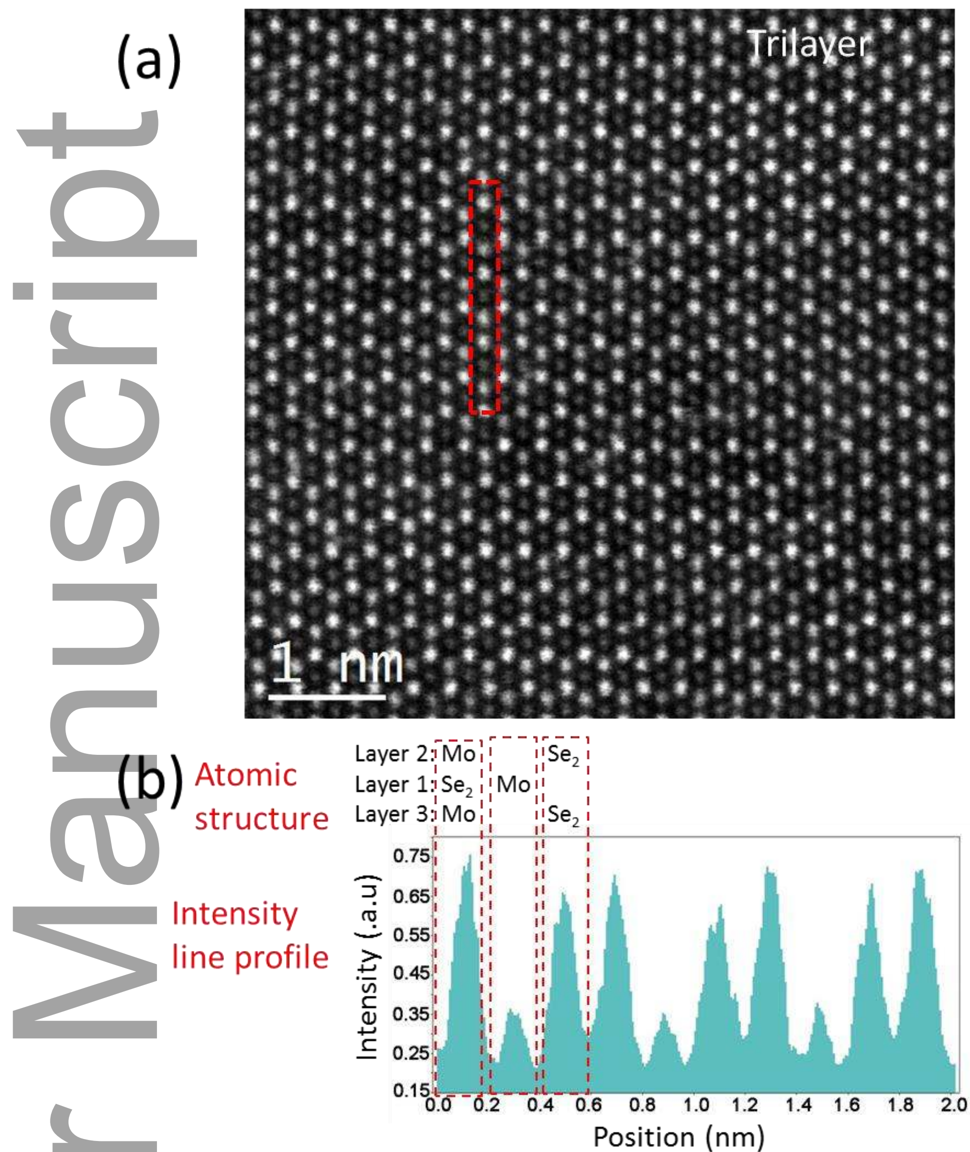

Figure S3. Z-contrast image of the 2-3 layer junction region (a) and trilayers (b) collected from 2-3 layer junction region. (c) Image intensity profile acquired along the red rectangle in the Z-contrast image above, indicating a 3R stacking in trilayer domain.

This article is protected by copyright. All rights reserved.

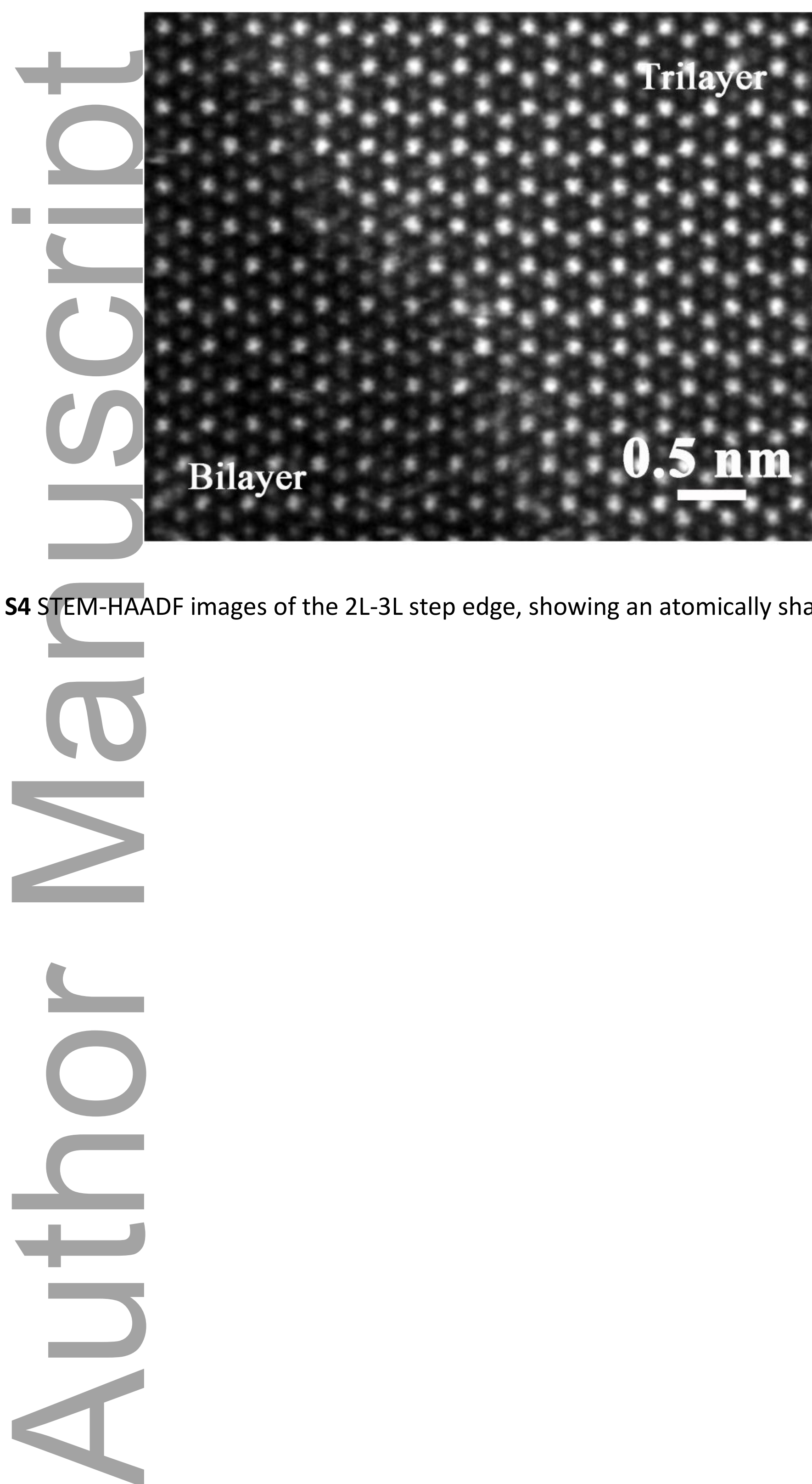

Figure S4 STEM-HAADF images of the 2L-3L step edge, showing an atomically sharp step.

Author Manuscript

This article is protected by copyright. All rights reserved.

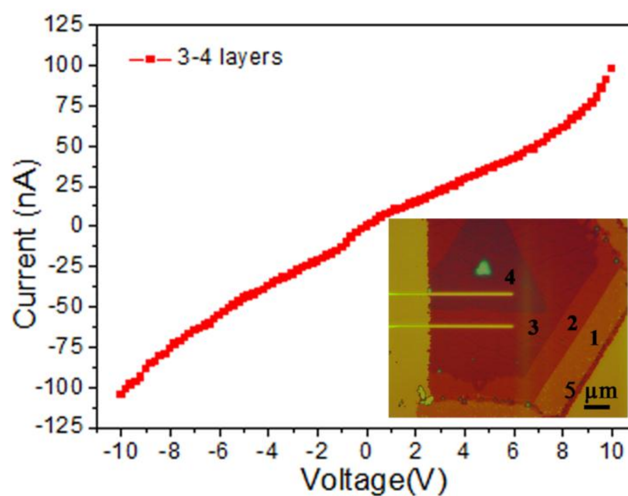

Figure S5. I-V curves of the device based 3-4 layer junction, showing no rectification characterization. Inset showing the optical image of the device based 3-4 layer junction, and each layer was marked by the number.

Author Manuscript

This article is protected by copyright. All rights reserved.

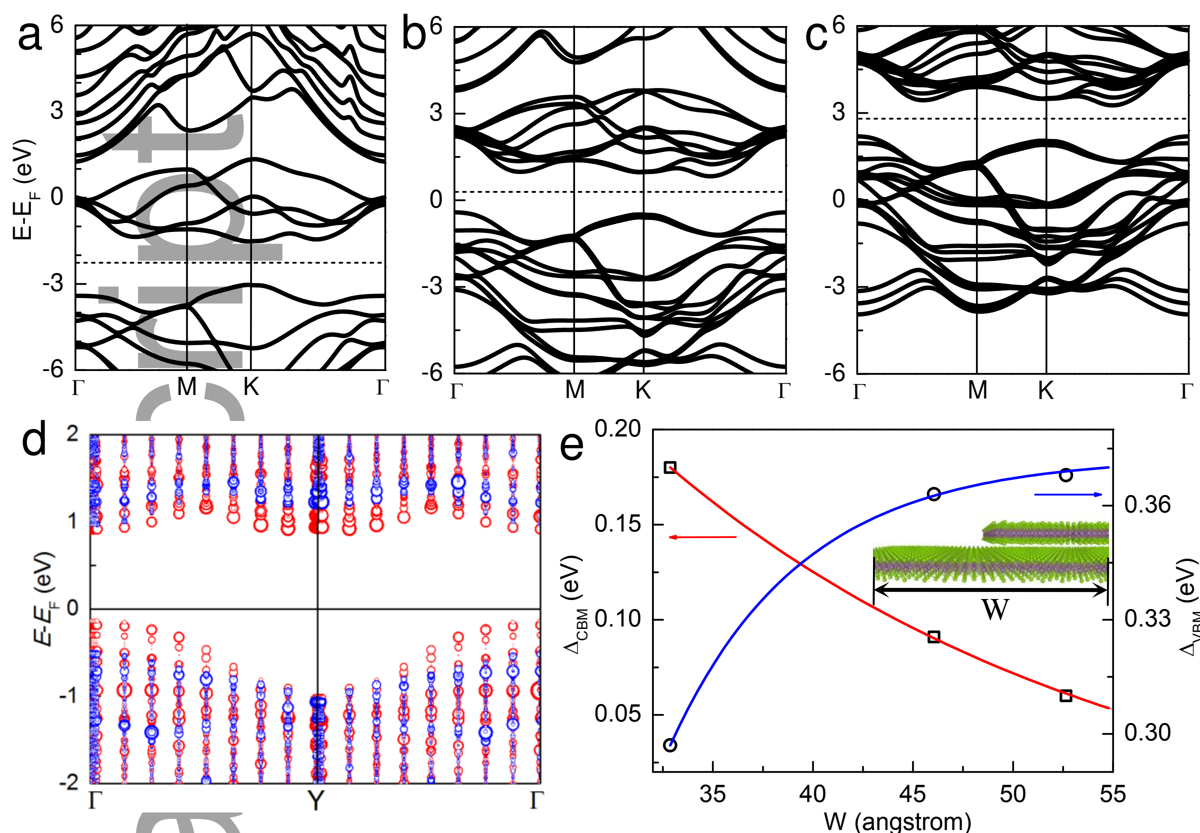

Figure S6. Electronic structure of the junction. (a-c) Band structure of freestanding (a) monolayer, (b) bilayer and (c) trilayer $MoSe_2$. (d) The band structure of the 1L-2L junction with a supercell size of 46 Å. The blue circles are for the bands projected to the atoms in middle of the 1L domain while the red ones are for those projected to the atoms in middle of the 1L domain. The circle size reflects the weight of the orbital components in the bands. The Fermi level is set to zero. (e) The differences between the conduction band minima (CBM) of the 1L and 2L as well as between the valence band maxima (VBM) of the 1L and 2L as a function of the width *W* of the supercell (see inset). Solid lines show the fitting results using exponential functions. $\Delta|_{W\to\infty}$ stands for the band offset cross the 1L-2L junction of experimental size and is calculated to be ~0.39 eV for the valence bands and ~-0.02 eV for the conduction bands of the 1L-2L junction.

Author Manuscript

This article is protected by copyright. All rights reserved.

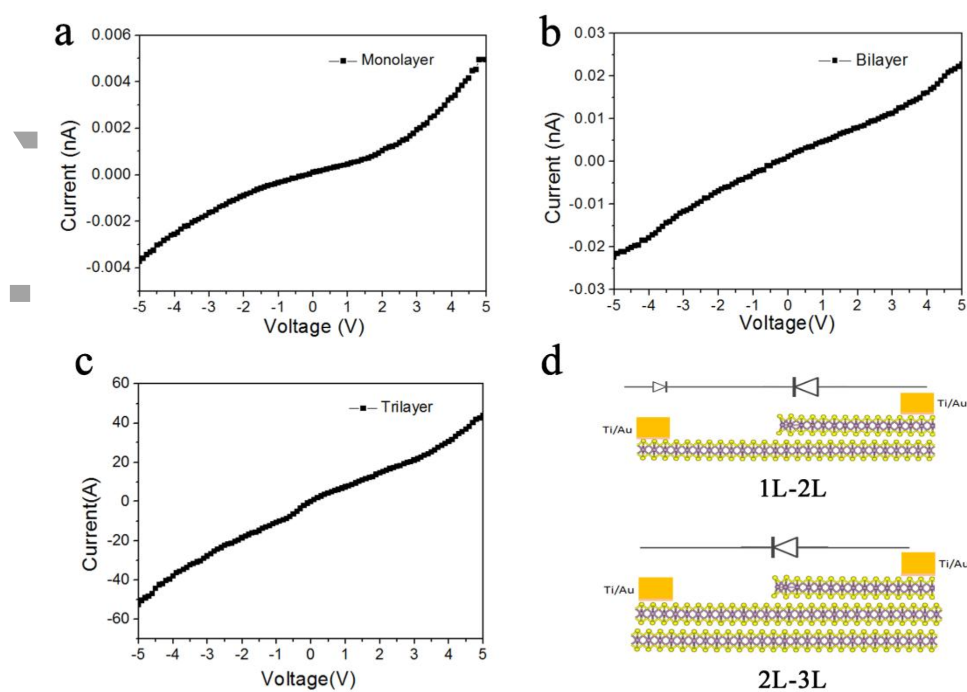

Figure S7 (a)-(b) Dark currents of individual monolayer, bilayer, and trilayer. (d) Schematic of the circuit based 1L-2L and 2L-3L junctions, respectively.

Author Manuscript

This article is protected by copyright. All rights reserved.

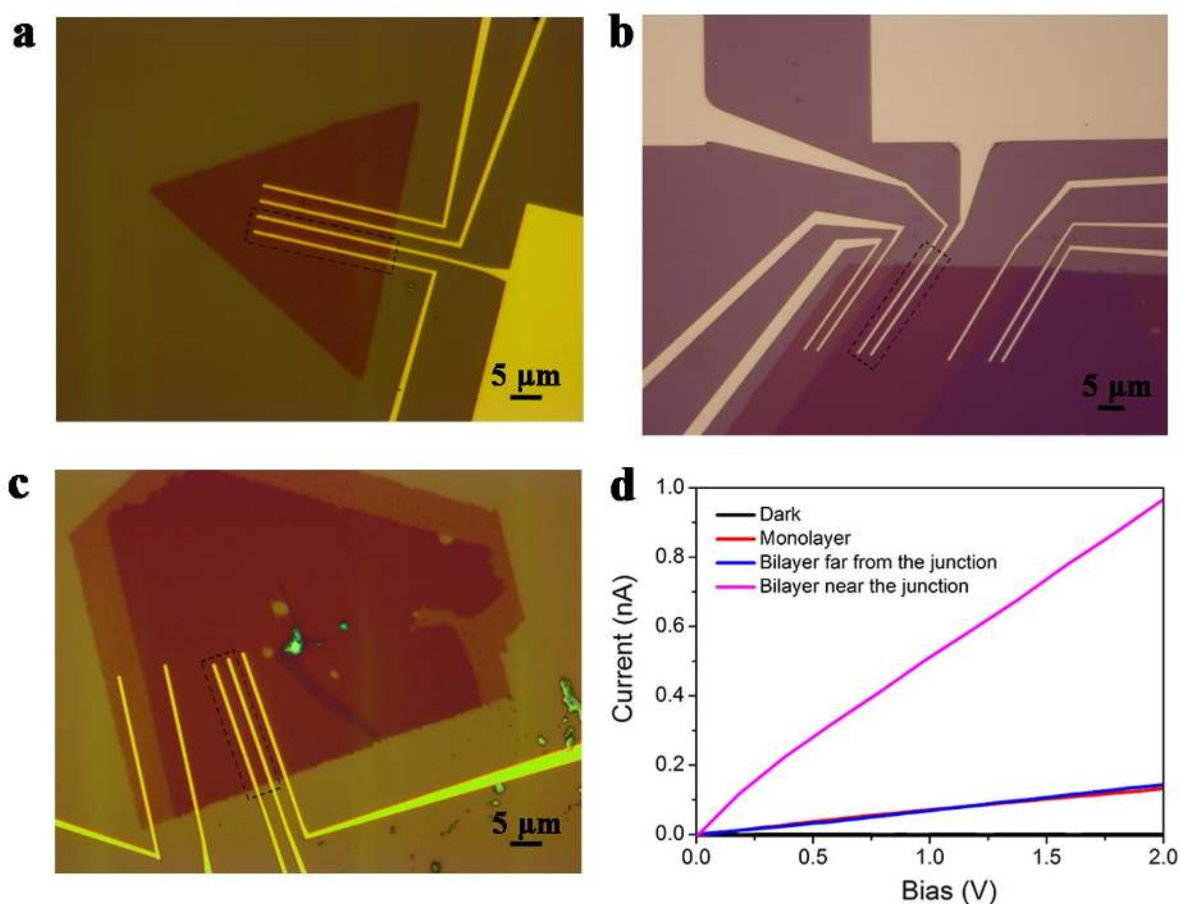

	Photocurrent (nA)	Darkcurrent (nA)	Area (μm^2)	Photoresponse (A/W)
1-1 layer	0.6	0	43.5954	0.001400895
2-2 layer (far)	0.585	0	43.8367	0.001358354
2-2 layer (near)	0.957	0	48.6968	0.010001759

Figure S8. a, b, and c Devices based on individual single layer (a), and bilayer near the junction (b) and far from the junction (c), in which all of them were marked by black dashed rectangle boxes. (d) Photoconductivity IV curves of devices based on individual single layer, and bilayer near the junction

Author Manuscript

This article is protected by copyright. All rights reserved.

and far from the junction under the same measurement condition. The table lists the compared data collected from photodetectors based on individual single layer, and bilayer near the junction and far from the junction. It can be observed that bilayer far from junction can deliver a comparable photoresponse to monolayer, and bilayer near the junction deliver a very higher photoresponse that those of bilayer far from junction and monolayer.

Author Manuscript

This article is protected by copyright. All rights reserved.

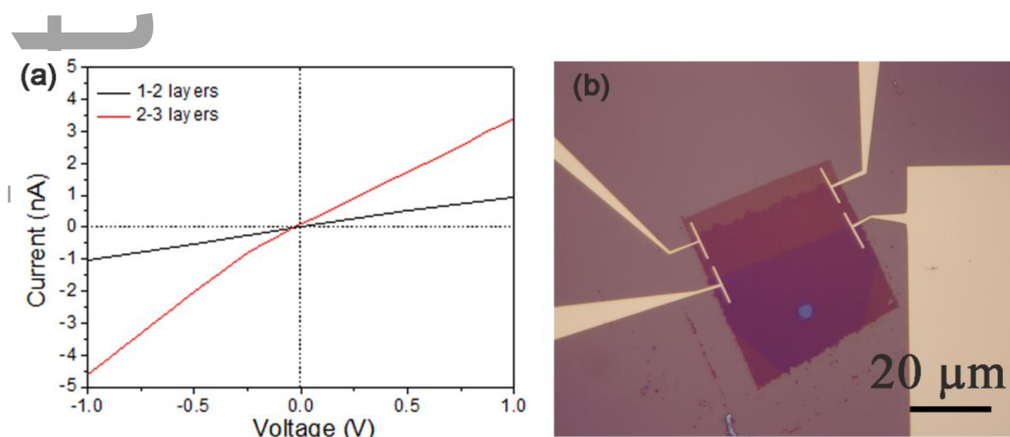

Figure S9. Photo-response based on the 1-2 layer and 2-3layer junction with a parallel direction along junction. (a) Photoconductivity IV curves of the devices, showing no photovoltaic response. (b)Optical images of the devices.

Photovoltaic vs. Photo-thermoelectric effects in "Layer Engineering" Junctions of TMDCs

We collected recent reported Seebeck coefficients of TMDCs at room temperature and zero gate voltage: for MoS_2, -1 ~ -2 mV/K[1, 2] and ~ -3.3 mV/K[3], for WSe_2, ~ 4.5mV/K[3]. Consulted from those works, we estimate the Seebeck coefficient of monolayer $MoSe_2$ at room temperature and zero gate voltage would be -0 ~ -10 mV/K. Because there is no report about the Seebeck coefficient of bilayer TMDCs, so here we can only estimate the Seebeck coefficient of bilayer $MoSe_2$ from two aspects. One is that we referred the Seebeck coefficient of monolayer and bilayer graphene, Xiaodong Xu et al reported their values are at the same order.[4] The other is that from the Seebeck coefficient

Author Manuscript

This article is protected by copyright. All rights reserved.

equation $S = -\frac{\pi^2 K_B^2 T}{3e} \frac{1}{G} \frac{dG}{dE}_{E=E_f}$ where the Seebeck coefficien can be calculated using the conductance data, and rewrote the equation $\frac{1}{G}\frac{dG}{dE} = \frac{I}{G}\frac{dG}{dV_g}\frac{dV_g}{dE}$. In a very recent review about electronic transport properties of transition metal dichalcogenide,[5] there is no obvious difference between monolayer and bilayer $MoSe_2$ FETs. Based on the above points, here we think that Seebeck coefficient difference ($\Delta S = S_{bilayer} - S_{monolayer}$) would be $<$10 mV/K. For the temperature difference, at the several µW powers used in our measurements it is very unlikely to be above 1K[1, 4, 6, 7]. Therefore, we evaluate the value of the photo-thermal voltage would be smaller than 10 mV from the equation ($\Delta V_{PTE} = \Delta S \Delta T$). If we compare this photo-thermal voltage value to the measured open-circuit voltage of 148 mV, it is clear that the photo-thermal contribution is very much smaller compared to the photovoltaic effect.

[1] M. Buscema, M. Barkelid, V. Zwiller, H. S. J. van der Zant, G. A. Steele, A. Castellanos-Gomez, *Nano Lett.*, **2013**, *13*, 358.

[2] J. Wu, H. Schmidt, K. K. Amara, X. Xu, G. Eda, B. Özyilmaz, *Nano Lett.*, **2014**, *14*, 2730.

[3] C.-H. Lee, G.-H. Lee, A. M. van der Zande, W. Chen, Y. Li, M. Han, X. Cui, G. Arefe, C. Nuckolls, T. F. Heinz, J. Guo, J. Hone, P. Kim, *Nat. Nanotechnol.*, **2014**, *9*, 676.

[4] X. Xu, N. M. Gabor, J. S. Alden, A. M. van der Zande, P. L. McEuen, *Nano Lett.*, **2010**, *10*, 562.

[5] H. Schmidt, F. Giustiniano, G. Eda, *Chem. Soc. Rev.*, **2015**, *44*, 7715.

[6] A. A. Balandin, S. Ghosh, W. Bao, I. Calizo, D. Teweldebrhan, F. Miao, C. N. Lau, *Nano Lett.*, **2008**, *8*, 902.

Author Manuscript

This article is protected by copyright. All rights reserved.

[7] N. M. Gabor, J. C. W. Song, Q. Ma, N. L. Nair, T. Taychatanapat, K. Watanabe, T. Taniguchi, L. S. Levitov, P. Jarillo-Herrero, *Science*, **2011**, *334*, 648.

Author Manuscript

The table of contents entry:

Based on this thickness dependence, a new concept for junction fabrication by connecting multiple regions with varying layer thicknesses is demonstrated. This type of junction is only possible in super thin layered 2D materials, and exhibits similar characteristics as p-n junctions. Rectification and photovoltaic effects are observed in chemically homogeneous $MoSe_2$ junctions between domains of different thicknesses.

Keyword: Layer engineering, 2D semiconductor junctions, Multilayer $MoSe_2$, Rectification effects, Photovoltaic effects

Yongmin He, Ali Sobhani , Sidong Lei, Zhuhua Zhang, Yongji Gong, Zehua Jin, Wu Zhou, Bo Li*, Yingchao Yang, Yuan Zhang, Xifan Wang, Boris Yakobson, Robert Vajtai, Naomi J. Halas, Erqing Xie*, Pulickel Ajayan*

Title: Layer engineering of 2D semiconductor junctions

ToC figure

This article is protected by copyright. All rights reserved.

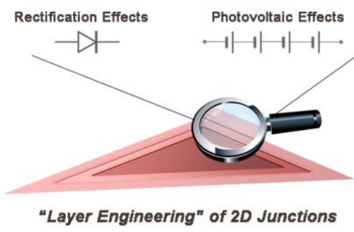

Author Manuscript

This article is protected by copyright. All rights reserved.